Dalton Transactions

PAPER

Cite this: *Dalton Trans.*, 2015, **44**, 11514

Double-malate bridging tri-lanthanoid cluster encapsulated arsenotungstates: syntheses, structures, luminescence and magnetic properties†

Pengtao Ma, Rong Wan, Yanan Si, Feng Hu, Yueyan Wang, Jingyang Niu* and Jingping Wang*

Five members of a new family of polyoxometalate (POM)-ligated trinuclear lanthanoid (Ln) clusters with the general formula $K_{20}Li_2[Ln_3(\mu_3\text{-}OH)(H_2O)_8(AsW_9O_{33})(AsW_{10}O_{35}(mal))]_2{\cdot}17H_2O$ [Ln = Dy (**1Dy**), Tb (**2Tb**), Gd (**3Gd**), Eu (**4Eu**), and Sm (**5Sm**), mal = malate] have been synthesized, all of which consist of the dimeric $\{[Ln_3(\mu_3\text{-}OH)(H_2O)_8(AsW_9O_{33})[AsW_{10}O_{35}(mal)]\}^{11-}$ polyanion constructed from a $\{AsW_9O_{33}\}$ and a $\{AsW_{10}O_{35}(mal)\}$ building block linked by a tri-Ln cluster $[Ln_3(\mu_3\text{-}OH)(H_2O)_8]^{8+}$, where the two malate ligands play a key bridging role. The $\{AsW_{10}O_{35}(mal)\}$ subunit can be viewed as the $\{AsW_9O_{33}\}$ building block anchoring an additional tungsten center $[WO_2(mal)]$. The electrospray ionization mass (ESI-MS) spectra indicate that the dimeric fragments of **1Dy** and **2Tb** are unstable, which are apt to produce the subunit $[KH_5Ln_3(OH)(H_2O)(AsW_9O_{33})_2]^{4-}$ in solution. The solid-state photoluminescence measurements display the yellowish green emission for **1Dy** and **5Sm**, green emission for **2Tb** and reddish orange emission for **4Eu**, which are attributed to the Ln^{III} f–f electron transitions. Magnetic property studies indicate that **1Dy** displays probable SMM behaviour with slow magnetization relaxation, whereas the weak antiferromagnetic interactions exist in two $\{Ln_3\}$ clusters for **2Tb–5Sm**.

Received 8th April 2015,
Accepted 11th May 2015

DOI: 10.1039/c5dt01323b

www.rsc.org/dalton

Introduction

Polyoxometalates (POMs) have attracted increasing attention because of their controllable shapes and sizes, versatile structural topologies, nucleophilic oxygen-enriched surface, high negative charges and rich electronic properties, which renders them excellent inorganic multidentate O-donor ligands for oxophilic d- and f-block metals to design and synthesize unique POM-based polynuclear transition metals (TM) or rare earth (RE) aggregates. Due to their structural and compositional diversity, allowing tuning of their electronic structures, POM-containing species have been found in diverse fields such as catalysis, medicine and magnetism.[1] Lanthanoid (Ln) centers with usual features including their higher coordination numbers, stronger oxophilicity, flexibility of coordination geometries and inherent properties such as luminescence and magnetic behaviors resulting from 4f electrons,[2] are particularly suitable for binding to POMs. Therefore, an emerging interest is that the combination of POMs and Ln clusters and/or Ln complexes gives rise to novel POM-based Ln complexes. In this field, lacunary polyoxotungstates (POTs) have attracted much attention. To date, a great number of POT derivatives with one or more Ln cations have been synthesized. The first Ln-containing POTs $[Ln(W_5O_{18})_2]^{n-}$ were reported by Peacock and Weakley in 1971, who synchronously explored the reaction of Ln ions and monolacunary Keggin-type POTs $[XW_{11}O_{39}]^{n-}$ ($X = Si^{IV}$, P^V) leading to the 1 : 1 and 1 : 2 derivatives.[3]

In the past several decades, an ongoing pursuit in POT chemistry is polynuclear Ln-containing giant POTs with nanoscopic size or high-nuclearity Ln aggregate encapsulated POT frameworks. A survey of already synthesized Ln-containing giant POTs (Table 1) indicates that only a handful of polynuclear Ln-containing POTs are known,[4] in which Ln ions are prone to incorporate into the lacunary sites of vacant POT precursors and/or to link two or more lacunary POT units resulting in large molecular assemblies. However, examples of Ln cluster sandwiched and/or encapsulated POTs are rare, despite many Ln coordination polymers and clusters emerging one

Key Laboratory of Polyoxometalate Chemistry of Henan Province, Institute of Molecular and Crystal Engineering, College of Chemistry and Chemical Engineering, Henan University, Kaifeng, Henan 475004, P. R. China. E-mail: jyniu@henu.edu.cn, jpwang@henu.edu.cn; Fax: (+86)-371-23886876

†Electronic supplementary information (ESI) available: Crystal structure figures (Fig. S1 and S2); IR spectra of **1Dy–5Sm** (Fig. S3); the excitation spectra (Fig. S4) and decay curves (Fig. S5); additional ac susceptibility of **1Dy** (Fig. S6), TG curves of **1Dy–5Sm** (Fig. S7); selected bond distances of **1Dy–5Sm** (Table S1) and BVS results of the protonated oxygen atoms (Table S2). CCDC 1043919–1043923 for **1Dy–5Sm**. See DOI: 10.1039/c5dt01323b

Table 1 Survey of already synthesized Ln-containing giant POTs

Formula	Number of Ln centers	Heteroatom	Ref.
$[Ce_{16}As_{12}W_{148}O_{524}(H_2O)_{36}]^{76-}$	16	As	Pope *et al.* (1997)[4a]
$[Ln_2(H_2O)_{10}P_8W_{48}O_{184}(H_4W_4O_{12})_2]^{26-}$ (Ln = La^{3+}, Ce^{3+}, Pr^{3+}, Nd^{3+})	2	P	Pope *et al.* (2007)[4b]
$[(Eu_2PW_{10}O_{38})_4(W_3O_{14})]^{30-}$	8	P	Francesconi *et al.* (2001)[4c]
$[Ce_3Sb_4W_2O_8(H_2O)_{10}(SbW_9O_{33})_4]^{19-}$	3	Sb	Gouzerh *et al.* (2002)[4d]
$[Eu_3(H_2O)_3(SbW_9O_{33})(W_5O_{18})_3]^{18-}$	3	Sb	Yamase *et al.* (1990)[4e]
$[K\subset\{Eu(H_2O)_2(\alpha\text{-}AsW_9O_{33})\}_6]^{35-}$	6	As	Yamase *et al.*(2003)[4f]
$[Cs\subset\{Eu(H_2O)_2(\alpha\text{-}AsW_9O_{33})\}_4]^{23-}$	4	As	Yamase *et al.* (2003)[4f]
$[Ce_{20}Ge_{10}W_{100}O_{376}(OH)_4(H_2O)_{30}]^{56-}$	20	Ge	Kortz *et al.* (2007)[4g]
$[Ho_5(H_2O)_{16}(OH)_2\ As_6W_{64}O_{220}]^{25-}$	5	As	Krebs *et al.* (2006)[4h]
$[Cs\subset Ln_6As_6W_{63}O_{218}(H_2O)_{14}(OH)_4]^{25-}$ (Ln = Eu^{3+}, Gd^{3+}, Tb^{3+}, Dy^{3+}, Ho^{3+}, Er^{3+})	6	As	Patzke *et al.* (2009)[4i]
$[Ln_{16}As_{16}W_{164}O_{576}(OH)_8(H_2O)_{42}]^{80-}$ (Ln = Eu^{3+}, Gd^{3+}, Tb^{3+}, and Ho^{3+})	16	As	Patzke *et al.*2011)[4j]
$[Gd_8As_{12}W_{124}O_{432}(H_2O)_{22}]^{60-}$	8	As	Patzke *et al.* (2009)[4k]
$[Gd_6As_6W_{65}O_{229}(OH)_4(H_2O)_{12}(OAc)_2]^{38-}$	6	As	Boskovic *et al.* (2009)[4l]
$[Yb_{10}As_{10}W_{88}O_{308}(OH)_8(H_2O)_{28}(OAc)_4]^{40-}$	10	As	Boskovic *et al.* (2009)[4l]
$[Tb_2(pic)(H_2O)_2(B\text{-}\beta\text{-}AsW_8O_{30})_2(WO_2(pic))_3]^{10-}$	2	As	Boskovic *et al.* (2010)[4m]
$[Tb_8(pic)_6(H_2O)_{22}(B\text{-}\beta\text{-}AsW_8\ O_{30})_4(WO_2(pic))_6]^{12-}$	8	As	Boskovic *et al.* (2010)[4m]
$[Ln_4As_5W_{40}O_{144}\ (H_2O)_{10}(gly)_2]^{21-}$	4	As	Boskovic *et al.* (2011)[4n]

after another.[5] Only a tiny amount of POT-ligated tri- or multi-Ln clusters were found in previous literature. The first complex of trilacunary Keggin derivative with tri-Ce cluster, $[(PW_9O_{34})_2Ce_3O_3(OH_2)_2]^{12-}$ was reported by Knoth in 1986.[6] In 2000, a tetranuclear Ce^{III} cluster $[Ce_4(OH)_2(H_2O)_9]^{10+}$ sandwiched POT $[Ce_4(OH)_2(H_2O)_9(P_2W_{16}O_{59})_2]^{14-}$ was isolated by Pope *et al.*[7] In 2003, Hill *et al.* communicated a trinuclear $[(YOH_2)_3(CO_3)]^+$ cluster sandwiched POT $[(YOH_2)_3(CO_3)\text{-}(A\text{-}\alpha\text{-}PW_9O_{34})_2]^{11-}$ with CO_3^{2-} encapsulated in the Y_3 plane,[8] and Tomsa *et al.* reported two Ln complexes $[(PW_9O_{34})_2Ln_3O_3(OH_2)_2]^{15-}$ (Ln = Ce^{3+}, La^{3+}).[9] In 2005, they reported two new POM-supported high-nuclearity Ln hydroxo/oxo clusters $[\{Y_4(\mu_3\text{-}OH)_4(H_2O)_8\}(\alpha\text{-}P_2W_{15}O_{56})_2]^{16-}$ and $[\{Yb_6(\mu_6\text{-}O)(\mu_3\text{-}OH)_6(H_2O)_6\}(\alpha\text{-}P_2W_{15}O_{56})_2]^{14-}$, which contain the tetranuclear $[Y_4(OH)_4]^{8+}$ cluster and the hexanuclear $[Yb_6(\mu_6\text{-}O)(\mu_3\text{-}OH)_6(H_2O)_6]^{10+}$ cluster encapsulated by two lacunary $[\alpha\text{-}P_2W_{15}O_{56}]^{12-}$ units, respectively.[10] In 2007, Wang *et al.* discovered a tetra-Ce cluster encapsulated POT aggregate $[Ce_4As_4W_{41}O_{149}]^{24-}$.[11] In 2010 and 2013, Khoshnavazi *et al.* synthesized a series of Ln sandwiched POMs $[(A\text{-}XW_9O_{34})_2(H_2OM)_3CO_3]^{n-}$ (X = Ge^{4+}, M = Y^{3+}, Sm^{3+}, Yb^{3+}; n = 13; X = P^{5+}, As^{5+}; M = Eu^{3+}, Gd^{3+}, Tb^{3+}, Dy^{3+}, Er^{3+}, n = 11).[12] Just recently, our group prepared a series of tartrate-functionalized tartar-Ln cluster sandwiched POTs $[Ln_2(C_4H_4O_6)(C_4H_2O_6)(AsW_9O_{33})]_2^{18-}$.[13] It is noteworthy that all these Ln cluster encapsulated POTs are almost purely inorganic; few Ln-organic cluster encapsulated POT aggregates are reported to date, although Ln-organic cation decorated POTs can be found everywhere. Therefore, it remains a serious challenge to explore the rational synthesis of high-nuclearity Ln cluster encapsulated POT aggregates.

Recently, we have been interested in exploring the assembly of high-nuclearity Ln clusters encapsulated in lacunary POTs in the presence of organic carboxylic acid ligands, thereby leading to new POT-ligated Ln clusters with a new functionality. In this work, we selected the dilacunary POT precursor $[As_2W_{19}O_{67}(H_2O)]^{14-}$ as the starting material for following considerations: (1) it possesses a large number of basic oxygen atoms on the lacunary site that are available to coordinate to Ln ions; (2) it can be degraded to the necessary POT subunits (such as {B-α-AsW_9O_{33}}, {B-β-AsW_9O_{33}}, and {B-β-$AsW_8O_{29}(OH)$}) for the assembly of new structural architectures; (3) the bridging {$WO(H_2O)$} linker in the precursor provides a fracture point where the molecule can be disassembled and reassembled, which is highly sensitive to the variation in reaction conditions. Synchronously, we are also targeting the incorporation of carboxylic acids as auxiliary ligands to access ternary Ln/organic/POM hybrid complexes, as these are known to facilitate the agglomeration of Ln centers into high-nuclearity clusters. Herein, we report five tungstoarsenate(III) containing double-malate bridging tri-Ln clusters: $K_{20}Li_2[Ln_3(\mu_3\text{-}OH)\text{-}(H_2O)_8(AsW_9O_{33})(AsW_{10}O_{35}(mal))]_2{\cdot}17H_2O$ [Ln = Dy (**1Dy**), Tb (**2Tb**), Gd (**3Gd**), Eu (**4Eu**), and Sm (**5Sm**), mal = malate], to our knowledge, which represent a rare family of POMs containing POT-ligated trinuclear or more Ln-organic clusters reported to date. Furthermore, the solid-state photoluminescence properties of **1Dy**, **2Tb**, **4Eu**, and **5Sm** were studied at room temperature, and their magnetic properties were investigated.

Results and discussion

Crystal structures

Single-crystal structural analyses reveal that the five compounds are almost isostructural and crystallize in the monoclinic space group $P2_1/n$. Therefore, only the structure of **1Dy** is described in detail. Their common structural feature is best described as a dimer constructed from two organic–inorganic hybrid tri-Ln cluster sandwiched arsenotungstate subunits $[Ln_3(\mu_3\text{-}OH)(H_2O)_8(AsW_9O_{33})(AsW_{10}O_{35}(mal))]^{11-}$, in which two mal ligands play a key bridging role in the construction of the structure. Complete single-crystal X-ray data for the five compounds are available in Table 2 and selected interatomic distances are provided in Table S1.† The bond-valence sum (BVS)

Table 2 Crystallographic data for **1Dy**–**5Sm**

	1Dy	2Tb	3Gd	4Eu	5Sm
Empirical formula	$C_8H_{74}As_4Dy_6K_{20}Li_2O_{181}W_{38}$	$C_8H_{74}As_4Tb_6K_{20}Li_2O_{181}W_{38}$	$C_8H_{74}As_4Gd_6K_{20}Li_2O_{181}W_{38}$	$C_8H_{74}As_4Eu_6K_{20}Li_2O_{181}W_{38}$	$C_8H_{74}As_4Sm_6K_{20}Li_2O_{181}W_{38}$
Formula weight	12 123.53	12 102.05	12 092.03	12 060.29	12 050.63
Crystal system	Monoclinic	Monoclinic	Monoclinic	Monoclinic	Monoclinic
Space group	$P2_1/n$	$P2_1/n$	$P2_1/n$	$P2_1/n$	$P2_1/n$
a [Å]	20.910(1)	20.924(3)	21.110(4)	21.063(11)	21.047(3)
b [Å]	25.333(2)	25.288(4)	25.441(5)	25.446(14)	25.429(3)
c [Å]	22.680(2)	22.707(4)	22.866(4)	22.740(12)	22.733(3)
β [°]	112.740(1)	112.785(3)	112.883(4)	112.625(9)	112.774(2)
V [Å^3]	11 080(1)	11 077(3)	11 314(4)	11 250(11)	11 218(3)
Z	2	2	2	2	2
ρ_{calcd} [g cm^{-3}]	3.634	3.628	3.549	3.560	3.568
μ [mm^{-1}]	22.692	22.588	22.000	22.029	21.984
Data/parameters	19 458/1110	19 474/1108	19 897/1106	19 740/1108	19 695/1109
R_{int}	0.0945	0.1049	0.1234	0.0621	0.0648
GOF	1.009	1.012	0.971	1.007	1.006
R_1, wR_2 [$I > 2\sigma(I)$]	0.0546, 0.1194	0.0688, 0.1686	0.0572, 0.1167	0.0429, 0.1037	0.0464, 0.1041
R_1, wR_2 [all data]	0.1106, 0.1448	0.1146, 0.2029	0.1429, 0.1490	0.0729, 0.1181	0.0890, 0.1217

calculations indicate that all of the W, As, and Ln atoms in the five compounds are in the +6, +3, and +3 oxidation states, respectively.[14]

The structural unit of **1Dy** consists of a double-mal bridging tri-Dy cluster encapsulated arsenotungstate fragment $[Dy_3(\mu_3\text{-}OH)(H_2O)_8(AsW_9O_{33})[AsW_{10}O_{35}(mal)]_2]^{22-}$, two Li^+ ions, twenty K^+ ions and seventeen lattice water molecules. As shown in Fig. 1a and Fig. S1,† the centrosymmetric fragment $[Dy_3(\mu_3\text{-}OH)(H_2O)_8\ (AsW_9O_{33})[AsW_{10}O_{35}(mal)]_2]^{22-}$ can be described as a dimeric assembly built by two sandwiched $[Dy_3(\mu_3\text{-}OH)(H_2O)_8(AsW_9O_{33})\ [AsW_{10}O_{35}(mal)]]^{11-}$ cores with two mal ligands serving as two "hinges". Alternatively, this fragment can also be viewed as a combination of two half-units $[Dy_3(\mu_3\text{-}OH)(H_2O)_8(AsW_9O_{33})\ [AsW_{10}O_{35}(mal)]]^{11-}$ related by an inversion center (0.5,0,1). Alternatively, the dimeric fragment is assembled by the $[AsW_9O_{33}]^{9-}$ and $[AsW_{10}O_{35}]^{7-}$ subunits together with trinuclear $[Dy_3(\mu_3\text{-}OH)(H_2O)_8(mal)]]^{6+}$ clusters (Fig. S2†). The asymmetric unit $[Dy_3(\mu_3\text{-}OH)(H_2O)_8(AsW_9O_{33})\text{-}[AsW_{10}O_{35}(mal)]]^{11-}$ (Fig. 1b) is composed of a triangular $\{Dy_3\}$

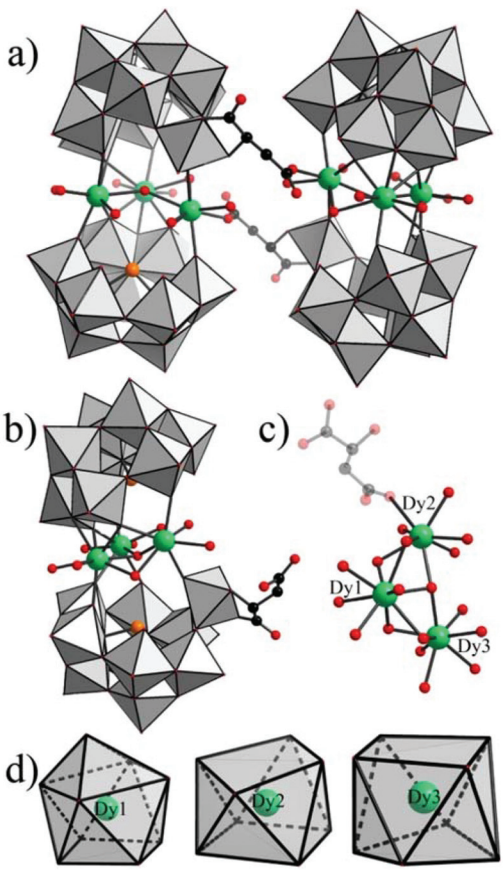

Fig. 1 (a) Ball-and-stick/polyhedral representation of dimeric polyanion for **1Dy**, (b) Ball-and-stick/polyhedral representation of asymmetric unit of **1Dy**, (c) Ball-and-stick representation of the $\{Dy_3\}$ cluster in **1Dy**, (d) The coordination environment around the three Dy^{III} cations. (Colour code: WO_6 = gray octahedra; Dy = green spheres; As = orange spheres; O = red spheres; C = black spheres, all the hydrogen atoms are omitted for clarity).

cluster sandwiched by a $[AsW_9O_{33}]^{9-}$ and a $[AsW_{10}O_{35}(mal)]^{10-}$ subunit. More interestingly, the hybrid subunit $[AsW_{10}O_{35}(mal)]^{10-}$ can be described as the product of a $\{WO_2(mal)\}$ moiety grafting to the $[AsW_9O_{33}]^{9-}$ subunit. Remarkably, at one end, the mal ligand coordinates to the $\{AsW_{10}\}$ group by one hydroxyl oxygen and one carboxylic oxygen atom, at the other end, it links to the $\{Dy_3\}$ cluster of the neighboring sandwiched subunit through another carboxylic oxygen atom. As a result, a double-mal bridging tri-Dy cluster sandwiched arsenotungstate dimer comes into being. As we know, it is difficult that the carboxylic oxygen atoms coordinate to the matrix of POMs,[11,15] although we reported a series of carboxylate-functionalized polyoxomolybdates.[16]

In the structure, a trinuclear cluster $[Dy_3(\mu_3\text{-}OH)(H_2O)_8]^{8+}$ links to a $[AsW_9O_{33}]^{9-}$ and a $[AsW_{10}O_{35}(mal)]^{10-}$ subunit. Three nonequivalent Dy atoms are joined together by a μ_3-oxo oxygen atom (O74), forming an irregular triangular arrangement (Fig. 1c), which can be approximately viewed as an isosceles triangle with two isosceles side lengths of (Dy1···Dy2) 3.623(2) and (Dy1···Dy3) 3.584(2) Å, and the bottom side (Dy2···Dy3) of 4.675(2) Å. This arrangement is obviously distinct from the other tri-Ln sandwiched POMs such as $[(A\text{-}XW_9O_{34})_2(H_2OM)_3CO_3]^{11-}$ (X = P^{5+}, As^{5+}; M = Tb^{3+}, Dy^{3+}, Er^{3+}),[12c] which presents a regular triangular Ln cluster with a CO_3^{2-} encapsulated in the center. The μ_3-oxo atom O74 is noncoplanar with the three Dy atoms' plane, and the distance between the O74 atom and the plane defined by three Dy atoms is 0.546 Å. In addition, the O74 atom is monoprotonated as is confirmed by BVS calculations with a BVS value of 0.977 (Table S2†).

Notably, three Dy^{3+} cations display two types of coordination geometries. The Dy1 ion inhibits in the nine-coordinate distorted monocapped square antiprism whereas the Dy2 and Dy3 ions adopt the eight-coordinate severely distorted square antiprismatic configuration (Fig. 1d and Table S1†). The difference in coordination geometries of Dy^{III} ions is related to the effect of the steric hindrance. The monocapped square antiprismatic geometry of the Dy1 ion is achieved by four terminal oxygen atoms (O42 and O48 from the $[AsW_9O_{33}]^{9-}$ subunit, O15 and O23 from the $[AsW_{10}O_{35}(mal)]^{10-}$ subunit) with Dy1–O(W) distances of 2.333(14)–2.615(14) Å, one μ_3-oxo oxygen atom (O74) [Dy1–O74: 2.385(14) Å], three water molecules (O1W, O2W and O3W) with Dy1–O(H_2O) distances of 2.422(16)–2.548(13) Å, and one bridging oxygen atom (O43) [Dy1–O43: 2.563(13) Å] from the $[AsW_9O_{33}]^{9-}$ subunit. The two bottom square planes for the Dy1 ion are respectively defined by the oxygen atoms O42, O48, O1W, O2W and O15, O23, O74, O3W, while the cap position is occupied by O43. The eight-coordinate Dy2 ion is coordinated to three available oxygen atoms (O35, O42, O73) [Dy2–O(W): 2.264(14)–2.344(14) Å] of the lacunary sites from the $[AsW_9O_{33}]^{9-}$ and the $[AsW_{10}O_{35}(mal)]^{10-}$ subunits, one sharing μ_3-oxo atom (O74) [Dy2–O74: 2.489(14) Å], three water molecules [Dy2–O(H_2O): 2.400(14)–2.446(16) Å], and one carboxylic oxygen atom (O39A, symmetry code: A, $-x + 1$, $-y$, $-z + 2$) [Dy2–O39A: 2.372(15) Å] contributed by a mal ligand. The square antiprismatic coordination sphere of the Dy3 ion is completed by four oxygen atoms (O23, O30, O48, and O56) [Dy3–O(W): 2.268(14)–2.532(14) Å] from the $[AsW_9O_{33}]^{9-}$ and $[AsW_{10}O_{35}(mal)]^{10-}$ subunits, one sharing μ_3-oxo atom (O74) [Dy3–O74: 2.385(13) Å], and three water molecules [Dy3–O(H_2O): 2.386(17)–2.455(16) Å]. For the two square antiprismatic geometries of Dy2 and Dy3 centers, two bottom square planes for the Dy2 ion are defined by the oxygen atoms O35, O39, O3W, O4W and O43, O73, O74, O5W, while two bottom square planes for the Dy3 ion are defined by the oxygen atoms O23, O30, O6W, O8W and O48, O56, O74, O7W. It should be emphasized that these planes are not strictly coplanar.

Infrared spectroscopy

The infrared spectra of the five compounds have been recorded between 4000 and 400 cm^{-1}, which are all similar with only slight shifts in the position of the bands (Fig. S3 in the ESI†). The terminal W–O_t obvious characteristic vibration appears at 944 cm^{-1} for **1Dy**, **2Tb** and **3Gd**, and at 943 cm^{-1} for **4Eu** and **5Sm**. The two types of W–O(–W) bridge stretching vibrations are seen as strong bands at 883 and 794 cm^{-1} for **1Dy**, at 881 and 793 cm^{-1} for **2Tb**, at 883 and 794 cm^{-1} for **3Gd**, at 884 and 791 cm^{-1} for **4Eu**, and at 884 and 793 cm^{-1} for **5Sm**. The peak around 720 cm^{-1} can be assigned to the W–O(–As) stretching vibration. In addition, the strong vibrations appearing at 3410 and 1626 cm^{-1} are assigned to the stretching vibration ν(O–H) and bending vibration δ(O–H) of free and coordinated water molecules, respectively. The mal carboxylate antisymmetric and symmetric stretching vibrations are observed at about 1628 and 1367 cm^{-1}, respectively, with the former band overlapping with the bending vibration δ(O–H) of the lattice and coordinated water molecules.[15] In comparison with uncoordinated carboxylate acid (about 1700 cm^{-1}), the $\nu_{as}(COO^-)$ vibrations of the five compounds all shift to low frequency as a result of the carboxylate coordination interaction with W atoms and Ln ions.

ESI-MS studies

In order to study the solution behavior of these nanosized clusters, the preliminary ESI-MS spectra of **1Dy** and **2Tb** in mixed methanol/water (1 : 1) solvent were recorded in the negative ion mode, both of which show a main signal for the −4 charged species appearing in the 1200–1400 m/z range. A comparison of the ESI-MS data by using single crystals of the two compounds is shown in Fig. 2. The two clusters display very similar spectra, but it is possible to see distinct differences between **1Dy** and **2Tb** in solution. The highest intensity signal appears at m/z = 1270.6 for **1Dy** and m/z = 1267.6 for **2Tb**, which are unambiguously attributed to the −4 charged species with formulae $[KH_5Dy_3(OH)(H_2O)(AsW_9O_{33})_2]^{4-}$ and $[KH_5Tb_3(OH)(H_2O)(AsW_9O_{33})_2]^{4-}$, respectively. The results indicate that the dimeric fragments of **1Dy** and **2Tb** are unstable compared with the parent cluster in the solid state, which are apt to produce the subunit $[KH_5Ln_3(OH)(H_2O)(AsW_9O_{33})_2]^{4-}$ in solution. Therefore, the $\{AsW_{10}O_{35}(mal)\}$ subunit is unstable in solution, in which the additional tungsten center

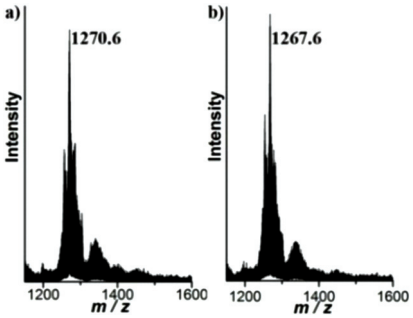

Fig. 2 Negative-mode ESI-MS of **1Dy** (a) and **2Tb** (b) in mixed H_2O/MeOH solvent (50%).

$[WO_2(mal)]$ is prone to escape from the $\{AsW_{10}O_{35}(mal)\}$ subunit forming a steady $\{AsW_9O_{33}\}$ fragment.

Luminescence properties

Excitation and luminescence spectra. The solid luminescence properties of **1Dy**, **2Tb**, **4Eu** and **5Sm** have been measured with their crystalline samples upon photoexcitation at room temperature. When monitored at the strongest emission, the excitation spectra of these compounds show a big distinction between 250 and 450 nm (Fig. S4†), which is closely related to the lanthanoid ions, resulting from their different intrinsic characteristics. In the case of **1Dy**, yellow luminescence was observed upon irradiation with a standard UV lamp (λ_{ex} = 366 nm). The typical luminescence peaks of Dy^{III} appear at 479, 573 and 662 nm (Fig. 3a). Two low-intensity emission peaks at 479 and 662 nm correspond to the $^4F_{9/2}\rightarrow{}^6H_{15/2}$ and $^4F_{9/2}\rightarrow{}^6H_{11/2}$, and the high-intensity emission peak at 573 nm is assigned to the $^4F_{9/2}\rightarrow{}^6H_{13/2}$, transitions of Dy^{3+} ions, respectively.[17] The excitation peak maximum was collected at 366 nm (Fig. S4a†) by monitoring the Dy(III) emission at 573 nm, which corresponds to the absorption by the f–f electron transitions of Dy^{III} ions. The yellow emission intensity of the $^4F_{9/2}\rightarrow{}^6H_{13/2}$ transition is strongest, which is related to the radiationless deactivation *via* cross relaxation of Dy^{III} ions, rather than the sensitization related to the POM-centered LMCT states; the emission quantum yield was found to be 27.5%. The phenomenon is similar to other Dy(III)-containing complexes.[17]

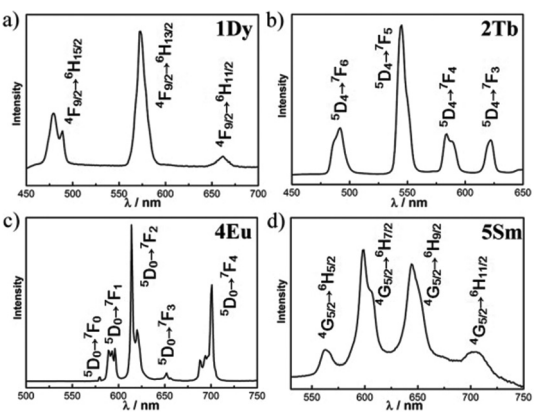

Fig. 3 The luminescence spectra of **1Dy** (a), **2Tb** (b), **4Eu** (c), and **5Sm** (d) in the solid state at room temperature.

For **2Tb**, the apparent emission peaks (Fig. 3b) at 491, 544, 584, 622 nm can be attributed to the $^5D_4\rightarrow{}^7F_6$, $^5D_4\rightarrow{}^7F_5$, $^5D_4\rightarrow{}^7F_4$, and $^5D_4\rightarrow{}^7F_3$ transitions, respectively, which correspond to the characteristic transitions from the $^5D_4$ excited state of the Tb^{III} ion to the ground-state ^7F_J (J = 6, 5, 4, 3) manifold.[18] Among them, the $^5D_4\rightarrow{}^7F_5$ transition is the strongest, suggesting predominant green luminescence with a quantum yield of 5.5%. The excitation spectrum of **2Tb** was collected by monitoring the Tb^{III} ion emission at 544 nm (Fig. S4b†). The excitation peak maximum was collected approximately at 378 nm in the UV region, which was attributed to the absorption of the Tb^{III} f–f electron transitions. This means that the sensitization of the Tb^{III} ions proceeds through the radiationless deactivation *via* cross relaxation of Tb^{III} ions, instead of the Tb^{IV}–W^V charge-transfer states or POM-centered LMCT states. This photoluminescence mainly originates from the f–f transitions of the Tb^{III} ions. This finding agrees well with the results of Yamase, who has shown that the sensitization of POM-centered LMCT states is not efficient for Tb^{III} ions due to the radiationless deactivation involving Tb^{IV}–W^V charge-transfer states.[19]

4Eu exhibits red photoluminescence under excitation at 395 nm (Fig. S4c†). The emission spectrum consists of emission bands involving in europium transitions from $^5D_0$ levels to its ^7F_J manifolds. (Fig. 3c) The emission bands at 580, 593, 614, 652, and 701 nm correspond to the $^5D_0\rightarrow{}^7F_0$, $^5D_0\rightarrow{}^7F_1$, $^5D_0\rightarrow{}^7F_2$, $^5D_0\rightarrow{}^7F_3$ and $^5D_0\rightarrow{}^7F_4$ transitions, respectively.[20] The $^5D_0\rightarrow{}^7F_2$ transition is the most intense emission, which leads to a bright reddish-orange emission with a high quantum yield of 16.5%. As we know, the magnetic dipole transition $^5D_0\rightarrow{}^7F_1$ is insensitive and hardly varies with the coordination environment, whereas the electric dipole transition $^5D_0\rightarrow{}^7F_2$ is a hypersensitive transition, whose intensity is very sensitive and apt to be influenced by the host environment.[21] We can obtain information on the site symmetry around the Eu^{III} ion and determine the local site symmetry from the ($^5D_0\rightarrow{}^7F_1$)/($^5D_0\rightarrow{}^7F_2$) emission intensity ratio.[20,22] The intensity of the $^5D_0\rightarrow{}^7F_2$ emission is obviously higher than that of the $^5D_0\rightarrow{}^7F_1$ emission, when Eu^{III} ions occupy non-inversion symmetry sites. In **4Eu**, the intensity of the $^5D_0\rightarrow{}^7F_2$ emission is observed to be significantly higher than that of the $^5D_0\rightarrow{}^7F_1$ transition, and the ($^5D_0\rightarrow{}^7F_1$)/($^5D_0\rightarrow{}^7F_2$) emission intensity ratio is relatively small (0.20), and therefore these Eu^{III} ions in **4Eu** mainly occupy sites without an inversion symmetry, which is in accordance with the result of its single crystal structure.

As for **5Sm**, four characteristic emission bands can be observed (Fig. 3d) under excitation at 403 nm (Fig. S4d†), which are ascribed to the $^4G_{5/2}\rightarrow{}^6H_J$ (J = 5/2, 7/2, 9/2, and 11/2), $^4G_{5/2}\rightarrow{}^6H_{5/2}$ (564 nm), $^4G_{5/2}\rightarrow{}^6H_{7/2}$ (598 nm), $^4G_{5/2}\rightarrow{}^6H_{9/2}$ (644 nm), and $^4G_{5/2}\rightarrow{}^6H_{11/2}$ (705 nm) transitions.[17d] The most intense peak of $^4G_{5/2}\rightarrow{}^6H_{7/2}$ transition appears at 598 nm,

leading to a strong yellowish green luminescence. The quantum yield of the Sm-centered luminescence reaches up to 38.4%.

Decay analysis. In order to obtain additional information on the luminescence properties, the lifetime measurements were employed at room temperature under strongest emission and excitation bands in the solid state. All the decay curves were well fitted by an exponential function (Fig. S5† and Table 3). For **1Dy**, **2Tb** and **5Sm**, they demonstrated the biexponential decay behavior with lifetimes of τ_1 = 3.91 μs (12%) and τ_2 = 14.39 μs (88%) for **1Dy**; τ_1 = 251.12 μs (86%) and τ_2 = 392.27 μs (14%) for **2Tb**; and τ_1 = 1.74 μs (38%) and τ_2 = 9.19 μs (62%) for **5Sm**. In contrast, the decay curve of **4Eu** exhibits single exponential behavior for the $^5D_0 \rightarrow {}^7F_2$ excited state, and the lifetime is τ = 292.25 μs. These results are comparable to other corresponding Ln^{III} complexes.[17a,17d,23]

CIE color chromaticity coordinates. The CIE 1931 (Commission International d'Eclairage) diagram is a universal method for studying all the possible colors by combining three primary colors, which has been extensively used to quantify the tunability of emission wavelength and the change in intensity of the emission bands. The white light emission is always located at the center of the CIE chromaticity diagram with the standard chromaticity coordinates (x = 0.33, y = 0.33). Thus, the chromaticity coordinates x and y are useful to determine the exact emission color of the samples. The emission spectra of **1Dy**, **2Tb**, **4Eu** and **5Sm** were converted into the x and y coordinates in the CIE chromaticity diagram, as presented in Fig. 4. The chromaticity coordinates (x, y) are found to be (0.371, 0.426), (0.353, 0.557), (0.650, 0.349), and (0.406, 0.402) corresponding to **1Dy**, **2Tb**, **4Eu** and **5Sm**, respectively. Therefore, the overall emission of the four samples is evaluated in terms of standard chromaticity diagram CIE, which can be easily seen to be yellowish green for **1Dy** and **5Sm**, green for **2Tb**, and reddish orange for **4Eu**. These results are close to those obtained for families of Ln-containing phosphors.[20,24]

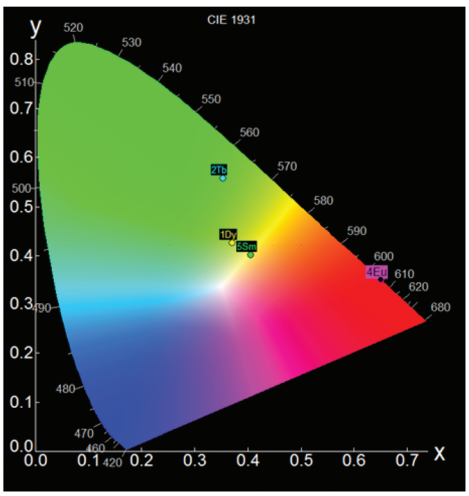

Fig. 4 CIE diagram of overall emission of **1Dy**, **2Tb**, **4Eu** and **5Sm**.

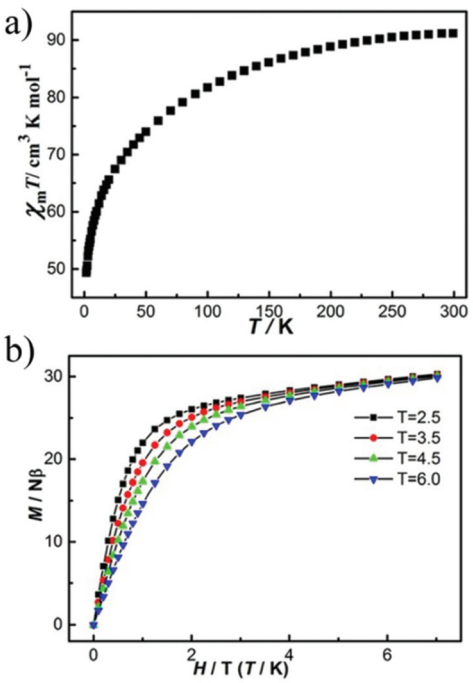

Fig. 5 (a) Temperature dependency of $\chi_M T$ in the range of 1.8–300 K in 100 Oe for **1Dy**. (b) Plot of magnetisation (M) of **1Dy** *versus* field between 2.5 and 6.0 K.

Magnetic properties

Static magnetic properties for 1Dy. The static magnetic susceptibility of **1Dy** was measured using a SQUID magnetometer in the temperature range of 1.8–300 K at 100 Oe (Fig. 5a). Direct-current (dc) magnetic susceptibility of **1Dy** was shown in the form of $\chi_M T$ *versus* T, where χ_M is the molar magnetic susceptibility. The room-temperature $\chi_M T$ value of 91.1 cm^3 mol^{-1} K is slightly higher than the theoretical value of 85.0 cm^3 mol^{-1} K expected for six non-interacting Dy^{III} ions (S = 5/2, L = 5, $^6H_{15/2}$, g = 4/3). Upon cooling, $\chi_M T$ continuously decreases and reaches a minimum of 49.3 cm^3 mol^{-1} K at 1.8 K. The thermal variation of $\chi_M T$ mainly depends on the populations of the Stark sublevels and/or the possible magnetic exchange between paramagnetic Dy^{III} ions in the system.

The magnetization *versus* field curve (Fig. 5b), measured below 6 K, shows a rapid increase in the magnetization at low fields, which does not reach saturation up to a field of 70 kOe.

Table 3 Photoluminescence lifetime data for **1Dy**, **2Tb**, **4Eu** and **5Sm**

	Lifetime (μs)	
Compound	τ_1	τ_2
1Dy	3.91(12%)	14.39 (88%)
2Tb	251.12 (86%)	392.27 (14%)
4Eu	292.25(100%)	
5Sm	1.74 (38%)	9.19 (62%)

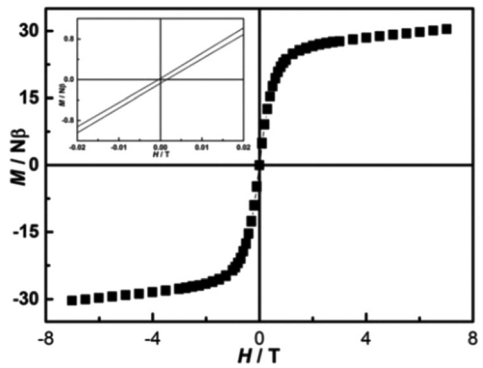

Fig. 6 Hysteresis loop for **1Dy** at 1.8 K. Inset: Expansion of hysteresis loops for **1Dy**.

The magnetization at 2.5 K increases very rapidly in the low field and reaches a value of *ca.* 30.3$N\beta$ at 70 kOe, whereas the magnetization at 6.0 K increases slowly as the magnetic field increases. The maximum value of 30.3$N\beta$ at 1.8 K and 70 kOe for **1Dy** is much lower than the theoretical saturation value of 60$N\beta$ for the two $\{Dy_3\}$ clusters. The unsaturated magnetization as well as the non-superposition of the *M versus H*/*T* curves suggests the large magneto-anisotropy and a low-lying excited state present in this system.[25] Interestingly, a small hysteresis loop is observed at 1.8 K with a coercive field (H_c) of 5 Oe and remnant magnetization (M_r) of 21 Oe emu mol^{-1} (Fig. 6), which confirmed possibly SMM behavior.

Alternating current magnetic susceptibility for 1Dy. In order to investigate the magnetization dynamics, alternating current (ac) magnetic susceptibility measurements were undertaken for **1Dy** in the temperature range 1.8–10 K under a zero static field. **1Dy** exhibits frequency-dependent in-phase and out-of-phase components, which indicates the probable SMM behavior. From temperature dependencies of the ac susceptibility (Fig. 7), **1Dy** clearly exhibits obvious temperature-dependent ac signals below 10 K. Without an external field, the out-of-phase signal (χ'') can be clearly increased with an increase of the frequency, although no maximum was observed down to 1.8 K, which is characteristic of the slow magnetization relaxation and the probable SMM behavior.[2c,18a] However, no maxima for χ'' were experimentally observed in the temperature and frequency range studied, thus we cannot determine the energy barrier and the corresponding relaxation time. This behavior is commonly reported for Ln-containing complexes.[26] To better understand the nature of dynamics, ac susceptibility measurements were carried out under different external fields in the range of 0–3000 Oe. From frequency dependencies of the ac susceptibility (Fig. S6†), both the in-phase (χ') and out-of-phase (χ'') signals do not reach the clearly defined maxima down to 1.8 K. The behavior mainly results from the more distorted coordination geometry in the $\{Dy_3\}$ cluster in **1Dy**, thus leading to the fast quantum tunneling from a more transverse anisotropy. We suspect that the magnetic coupling interactions in the $\{Dy_3\}$ cluster play a dominant role.

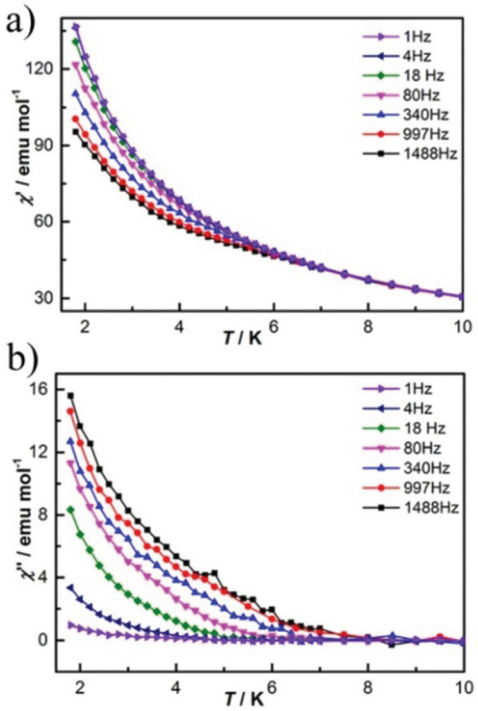

Fig. 7 Temperature dependency of the in-phase (χ') (a) and out-of-phase (χ'') (b) signals from the ac susceptibility measurements of **1Dy** without an applied static field.

Static magnetic properties for 2Tb–5Sm. Variable temperature magnetic susceptibilities of **2Tb–5Sm** were measured from 300 to 1.8 K in an applied field of 1 kOe (Fig. 8). For **2Tb**, the value of $\chi_M T$ is 70.94 cm^3 mol^{-1} K at 300 K, close to the expected value of 70.86 cm^3 K mol^{-1} for six Tb^{III} ions ($^7F_6$, g = 3/2). On lowering of the temperature, $\chi_M T$ gradually decreases to a value of 36.73 cm^3 K mol^{-1} at 1.8 K.

For **3Gd**, the isotropic f^7 Gd ion has no orbital contribution. The $\chi_M T$ value is 47.69 cm^3 K mol^{-1} at 300 K, which is consistent with the spin only value of 47.25 cm^3 K mol^{-1}

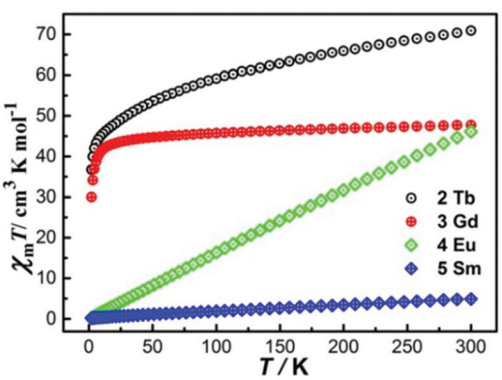

Fig. 8 Temperature dependence of the $\chi_M T$ product at 1000 Oe for **2Tb**, **3Gd**, **4Eu**, and **5Sm**.

expected for six non-interacting Gd^{3+} ions ($S = 7/2$, $L = 0$, $^8S_{7/2}$, $g = 2$, $C = 7.875$ cm^3 K mol^{-1}).[27] Upon cooling, the $\chi_M T$ product remains fairly constant down to around 50 K before dropping rapidly down to 30.2 cm^3 K mol^{-1} at 1.8 K.

Different from most of the trivalent Ln ions, the first excited state of the Eu^{III} and Sm^{III} ions may be thermally populated because of the small energy separation [400 cm^{-1} for Eu^{III} and 1000 cm^{-1} for Sm^{III}]. Therefore, the crystal field effect and the possible thermal population of the higher energy state should be taken into account for Eu^{III}- and Sm^{III}-containing POMs. For **4Eu**, the $\chi_M T$ values gradually decrease from 46.11 cm^3 K mol^{-1} at 300 K to 0.36 cm^3 K mol^{-1} at 1.8 K, which should be attributed to the depopulation of the Stark levels for Eu^{III} ions.[28]

As for **5Sm**, the $\chi_M T$ values gradually decreases from 4.91 cm^3 K mol^{-1} at 300 K to 0.19 cm^3 K mol^{-1} at 1.8 K. The minimum value of 0.19 cm^3 K mol^{-1} at 2 K is evidently smaller than that for six noninteracting Sm^{III} ions (0.534 cm^3 K mol^{-1}), indicating the occurrence of weak antiferromagnetic interactions of the six Sm^{III} ions within the two $\{Sm_3\}$ clusters mediated by bridge-oxygen atoms as well as the spin–orbital coupling and the crystal field effect. This observation has been encountered in our previously reported Sm^{III}-containing POMs.[28b]

Experimental

Materials and methods

$K_{14}[As_2W_{19}O_{67}(H_2O)]$ was prepared according to the reference[29] and confirmed by IR spectrum. Other chemical reagents were purchased and used without further purification. Elemental analyses (C, H) were conducted on a Perkin-Elmer 2400-II CHNS/O analyzer. IR spectra were recorded on a Bruker VERTEX 70 IR spectrometer using KBr pellets in the range of 4000–400 cm^{-1}. ICP analyses were performed on a Perkin-Elmer Optima 2000 ICP–OES spectrometer. ESI-MS spectrometry was carried out with Bruker MTQ III-QTOF. The experiments were performed with the negative ion mode in mixed methanol/water (1 : 1) solvent by direct infusion with a syringe pump with a flow rate of 5 μL min^{-1}. Photoluminescence properties were recorded on an EDINBURGH FLS980 fluorescence spectrophotometer. Variable-temperature magnetic susceptibility data were obtained on a SQUID magnetometer (Quantum Design, MPMS-VSM) in the temperature range of 1.8–300 K. TG analyses were performed on a Perkin-Elmer TGA7 instrument in flowing N_2 with a heating rate of 10 °C min^{-1}.

Syntheses of 1Dy. The representative synthesis of **1Dy** was performed as follows: a sample of $K_{14}[As_2W_{19}O_{67}(H_2O)]$ (1.32 g, 0.25 mmol) was added under stirring to a solution of 0.14 g DL-malic acid (1.04 mmol) and $DyCl_3{\cdot}6H_2O$ (0.22 g, 0.60 mmol) in 40 mL distilled water; ten minutes later, the pH of the solution was adjusted to about 7.0 with 3.0 mol L^{-1} lithium hydroxide solution and then the mixture was heated to 60 °C for 1 h. After being cooled to room temperature, the clear solution was made to stand for crystallization. Colorless block crystals were collected after about two weeks. Yield: 0.76 g (31% based on $DyCl_3{\cdot}6H_2O$). Elemental analysis (%) calcd for **1Dy**: C, 0.79; H, 0.62; Li, 0.11; K, 6.45; As, 2.47; Dy, 8.04; W, 57.63. Found: C, 0.69; H, 0.77; Li, 0.09; K, 6.32; As, 2.36; Dy, 7.86; W, 56.37. Selected IR (KBr, cm^{-1}): 3410 (br), 1627 (s), 1367 (w), 944 (s), 883 (s), 749 (s), 717 (s).

Synthesis of 2Tb. The synthesis of **2Tb** is similar to **1Dy** but with $TbCl_3{\cdot}6H_2O$ (0.22 g, 0.60 mmol) instead of $DyCl_3{\cdot}6H_2O$. Yield: 0.66 g (27% based on $TbCl_3{\cdot}6H_2O$). Elemental analysis (%) calcd for **2Tb**: C, 0.79; H, 0.62; Li, 0.11; K, 6.46; As, 2.48; Tb, 7.88; W, 57.73. Found: C, 0.70; H, 0.74; Li, 0.08; K, 6.30; As, 2.35; Tb, 7.60; W, 56.75. Selected IR (KBr, cm^{-1}): 3413 (br), 1628 (s), 1369 (w), 1369 (w), 944 (s), 881 (s), 793 (s), 720 (s).

Synthesis of 3Gd. The synthesis of **3Gd** is similar to **1Dy** but with $GdCl_3{\cdot}6H_2O$ (0.22 g, 0.60 mmol) instead of $DyCl_3{\cdot}6H_2O$. Yield: 0.27 g (11% based on $GdCl_3{\cdot}6H_2O$). Elemental analysis (%) calcd for **3Gd**: C, 0.79; H, 0.62; Li, 0.11; K, 6.47; As, 2.48; Gd, 7.80; W, 57.78. Found: C, 0.68; H, 0.76; Li, 0.09; K, 6.29; As, 2.38; Gd, 7.63; W, 56.54. Selected IR (KBr, cm^{-1}): 3409 (br), 1367 (w), 944 (s), 883 (s), 794 (s), 718 (s).

Synthesis of 4Eu. The synthesis of **4Eu** is similar to **1Dy** but with $EuCl_3{\cdot}6H_2O$ (0.22 g, 0.60 mmol) instead of $DyCl_3{\cdot}6H_2O$. Yield: 0.58 g (24% based on $EuCl_3{\cdot}6H_2O$). Elemental analysis (%) calcd for **4Eu**: C, 0.80; H, 0.62; Li, 0.11; K, 6.48; As, 2.49; Eu, 7.56; W, 57.93. Found: C, 0.70; H, 0.75; Li, 0.08; K, 6.32; As, 2.36; Eu, 7.39; W, 56.57. Selected IR (KBr, cm^{-1}): 3413 (br), 1627 (s), 1366 (w), 943 (s), 884 (s), 791 (s), 720 (s).

Synthesis of 5Sm. The synthesis of **5Sm** is similar to **1Dy** but with $SmCl_3{\cdot}6H_2O$ (0.22 g, 0.60 mmo) instead of $DyCl_3{\cdot}6H_2O$. Yield: 0.31 g (13% based on $SmCl_3{\cdot}6H_2O$). Elemental analysis (%) calcd for **5Sm**: C, 0.80; H, 0.62; Li, 0.12; K, 6.49; As, 2.49; Sm, 7.49; W, 57.97. Found: C, 0.72; H, 0.76; Li, 0.09; K, 6.33; As, 2.39; Sm, 7.20; W, 56.51. Selected IR (KBr, cm^{-1}): 3412 (br), 1626 (s), 1367 (w), 943 (s), 884 (s), 793 (s), 721 (s).

X-ray crystallographic

Single crystals of the five compounds were stilled in a capillary tube when prepared for data collection at 296(2) K as they weather easily. Indexing and data collection were performed on a Bruker D8 SMART APEX II CCD diffractometer with graphite-monochromated Mo Kα radiation (λ = 0.71073 Å). This data reduction included a correction for Lorentz and polarization effects, with an applied multi-scan absorption correction SADABS program.[30] Direct methods (SHELXS97) successfully located the tungsten atoms, and successive Fourier syntheses (SHELXL97) revealed the remaining atoms.[31] Refinements were done using full-matrix least-squares against F^2 on all data. In the final refinement, the W, As, lanthanoid, K, C and most O atoms were refined anisotropically; the water O atoms as well as the disordered K countercations were refined isotropically. The hydrogen atoms of the malate groups were placed in calculated positions and then refined using a riding model. All H atoms on water molecules were directly included in the molecular formula.

Conclusions

In summary, a rare family of POMs containing POT-ligated multinuclear Ln-organic tungstoarsenate(III) clusters $[Ln_3(\mu_3\text{-}OH)(H_2O)_8(AsW_9O_{33})(AsW_{10}O_{35}(mal))]_2^{22-}$ [Ln = Dy (**1Dy**), Tb (**2Tb**), Gd (**3Gd**), Eu (**4Eu**), and Sm (**5Sm**), mal = malate] was synthesized by the routine solution method. The five compounds display a novel dimeric skeleton built by two tri-Ln sandwiched tungstoarsenate clusters linked by double-mal bridges. ESI-MS studies of **1Dy** and **2Tb** indicate that the dimeric polyanions tend to decompose into a stable subunit $[KH_5Ln_3(OH)(H_2O)(AsW_9O_{33})_2]^{4-}$ in solution, demonstrating that the additional tungsten center $[WO_2(mal)]$ is unstable and liable to escape from the $\{AsW_{10}O_{35}(mal)\}$ subunit. The characteristic fluorescence emissions of **1Dy**, **2Tb**, **4Eu** and **5Sm** are derived from the nature of rare earth cations. The preliminary magnetic studies indicate that **1Dy** displays the probable SMM behavior. The successful preparations of these Ln-organic tungstoarsenates demonstrate that the combination of lacunary POMs and Ln clusters in the presence of organic polycarboxylic acid may be a feasible strategy to design and synthesize novel Ln-organic cluster encapsulated POM aggregates under rational solution conditions and provide new insight for designing responsive multifunctional materials based on POMs and Ln complexes. In other words, it is reasonable to believe that the present work will be important significantly in expanding the study and exploration of Ln-containing POM-based function materials.

Acknowledgements

We gratefully acknowledge support from the NSFC and the Foundation of Education Department of Henan Province (no. 14A150028).

Notes and references

1 (*a*) M. T. Pope and A. Müller, *Angew. Chem., Int. Ed. Engl.*, 1991, **30**, 34–48; (*b*) I. V. Kozhevnikov, *Chem. Rev.*, 1998, **98**, 171–198; (*c*) N. Mizuno and M. Misono, *Chem. Rev.*, 1998, **98**, 199–218; (*d*) C. L. Hill, *J. Mol. Catal. A: Chem.*, 2007, **262**, 2–6; (*e*) M. T. Pope and A. Müller, *Polyoxometalates: From Platonic Solids to Anti-Retroviral Activity*, Kluwer Academic Publishers, Dordrecht, Netherlands, 1994, pp. 1–411; (*f*) J. T. Rhule, C. L. Hill, D. A. Judd and R. F. Schinazi, *Chem. Rev.*, 1998, **98**, 327–358; (*g*) J. M. Clemente-Juan and E. Coronado, *Coord. Chem. Rev.*, 1999, **193–195**, 361–394; (*h*) U. Kortz, A. Müller, J. van Slageren, J. Schnack, N. S. Dalal and M. Dressel, *Coord. Chem. Rev.*, 2009, **253**, 2315–2327.

2 (*a*) Z. Li, G. Zhu, X. Guo, X. Zhao, Z. Jin and S. Qiu, *Inorg. Chem.*, 2007, **46**, 5174–5178; (*b*) A. H. Yang, J. Y. Zou, W. M. Wang, X. Y. Shi, H. L. Gao, J. Z. Cui and B. Zhao, *Inorg. Chem.*, 2014, **53**, 7092–7100; (*c*) D. N. Woodruff, R. E. Winpenny and R. A. Layfield, *Chem. Rev.*, 2013, **113**, 5110–5148; (*d*) M. Vonci and C. Boskovic, *Aust. J. Chem.*, 2014, **67**, 1542–1552.

3 (*a*) R. D. Peacock and T. J. R. Weakley, *J. Chem. Soc. A*, 1971, 1836–1839; (*b*) R. D. Peacock and T. J. R. Weakley, *J. Chem. Soc. A*, 1971, 1937–1940.

4 (*a*) K. Wassermann, M. H. Dickman and M. T. Pope, *Angew. Chem., Int. Ed. Engl.*, 1997, **36**, 1445–1448; (*b*) M. Zimmermann, N. Belai, R. J. Butcher, M. T. Pope, E. V. Chubarova, M. H. Dickman and U. Kortz, *Inorg. Chem.*, 2007, **46**, 1737–1740; (*c*) R. C. Howell, F. G. Perez, S. Jain, J. W. De Horrocks, A. L. Rheingold and L. C. Francesconi, *Angew. Chem., Int. Ed.*, 2001, **40**, 4031–4034; (*d*) G. Xue, J. Vaissermann and P. Gouzerh, *J. Cluster Sci.*, 2002, **13**, 409–421; (*e*) T. Yamase, H. Naruke and Y. Sasaki, *J. Chem. Soc., Dalton Trans.*, 1990, 1687–1696; (*f*) K. Fukaya and T. Yamase, *Angew. Chem., Int. Ed.*, 2003, **42**, 654–658; (*g*) B. S. Bassil, M. H. Dickman, I. Römer, B. von der Kammer and U. Kortz, *Angew. Chem., Int. Ed.*, 2007, **46**, 5985–5985; (*h*) D. Drewes, M. Piepenbrink and B. Krebs, *Z. Anorg. Allg. Chem.*, 2006, **632**, 534–536; (*i*) F. Hussain, B. Spingler, F. Conrad, M. Speldrich, P. Kogerler, C. Boskovic and G. R. Patzke, *Dalton Trans.*, 2009, 4423–4425; (*j*) F. Hussain and G. R. Patzke, *CrystEngComm*, 2011, **13**, 530; (*k*) F. Hussain, F. Conrad and G. R. Patzke, *Angew. Chem., Int. Ed.*, 2009, **48**, 9088–9091; (*l*) F. Hussain, R. W. Gable, M. Speldrich, P. Kogerler and C. Boskovic, *Chem. Commun.*, 2009, 328–330; (*m*) C. Ritchie, E. G. Moore, M. Speldrich, P. Kögerler and C. Boskovic, *Angew. Chem., Int. Ed.*, 2010, **49**, 7702–7705; (*n*) C. Ritchie, M. Speldrich, R. W. Gable, L. Sorace, P. Kogerler and C. Boskovic, *Inorg. Chem.*, 2011, **50**, 7004–7014.

5 (*a*) F. S. Guo, J. D. Leng, J. L. Liu, Z. S. Meng and M. L. Tong, *Inorg. Chem.*, 2012, **51**, 405–413; (*b*) W. H. Fang, L. Cheng, L. Huang and G. Y. Yang, *Inorg. Chem.*, 2013, **52**, 6–8; (*c*) C. Hennig, A. Ikeda-Ohno, W. Kraus, S. Weiss, P. Pattison, H. Emerich, P. M. Abdala and A. C. Scheinost, *Inorg. Chem.*, 2013, **52**, 11734–11743; (*d*) D. T. Thielemann, A. T. Wagner, E. Rosch, D. K. Kolmel, J. G. Heck, B. Rudat, M. Neumaier, C. Feldmann, U. Schepers, S. Brase and P. W. Roesky, *J. Am. Chem. Soc.*, 2013, **135**, 7454–7457; (*e*) A. B. Canaj, G. K. Tsikalas, A. Philippidis, A. Spyros and C. J. Milios, *Dalton Trans.*, 2014, **43**, 12486–12494; (*f*) D. M. Pajerowski, Q. Li, J. Hyun, C. L. Dennis, D. Phelan, P. Yan, P. Chen and G. Li, *Dalton Trans.*, 2014, **43**, 11973–11980.

6 W. H. Knoth, P. J. Domaille and R. L. Harlow, *Inorg. Chem.*, 1986, **25**, 1577–1584.

7 A. Ostuni and M. T. Pope, *Sci. Paris, Série IIc, Chimie: Chem.*, 2000, **3**, 199–204.

8 X. Fang, T. M. Anderson, W. A. Neiwert and C. L. Hill, *Inorg. Chem.*, 2003, **42**, 8600–8602.

9 A.-R. Tomsa, L. Muresan, A. Koutsodimou, P. Falaras and M. Rusu, *Polyhedron*, 2003, **22**, 2901–2909.

10 X. Fang, T. M. Anderson, C. Benelli and C. L. Hill, *Chem. – Eur. J.*, 2005, **11**, 712–718.

11 W. Chen, Y. Li, Y. Wang, E. Wang and Z. Su, *Dalton Trans.*, 2007, 4293–4301.

12 (*a*) R. Khoshnavazi and S. Tayamon, *J. Coord. Chem.*, 2010, **63**, 3356–3364; (*b*) R. Khoshnavazi and S. Gholamyan, *J. Coord. Chem.*, 2010, **63**, 3365–3372; (*c*) R. Khoshnavazi, F. Nicolò, H. Amiri Rudbari, E. Naseri and A. Aminipour, *J. Coord. Chem.*, 2013, **66**, 1374–1383.

13 Y. Wang, X. Sun, S. Li, P. Ma, J. Wang and J. Niu, *Dalton Trans.*, 2015, **44**, 733–738.

14 I. D. Brown and D. Altermatt, *Acta Crystallogr., Sect. B: Struct. Sci.*, 1985, **B41**, 244–247.

15 C. Ritchie, V. Baslon, E. G. Moore, C. Reber and C. Boskovic, *Inorg. Chem.*, 2012, **51**, 1142–1151.

16 (*a*) D. Yang, S. Li, P. Ma, J. Wang and J. Niu, *Inorg. Chem.*, 2013, **52**, 8987–8992; (*b*) D. Yang, S. Li, P. Ma, J. Wang and J. Niu, *Inorg. Chem.*, 2013, **52**, 14034–14039; (*c*) D. Yang, Y. Liang, P. Ma, S. Li, J. Wang and J. Niu, *Inorg. Chem.*, 2014, **53**, 3048–3053; (*d*) D. Yang, Y. Liang, P. Ma, S. Li, J. Wang and J. Niu, *CrystEngComm*, 2014, **16**, 8041–8046.

17 (*a*) Y.-L. Wang, B. Gu, Y. Ma, C. Xing, Q.-L. Wang, L.-C. Li, P. Cheng and D.-Z. Liao, *CrystEngComm*, 2014, **16**, 2283–2289; (*b*) Y.-L. Wang, Y. Ma, X. Yang, J. Tang, P. Cheng, Q.-L. Wang, L.-C. Li and D.-Z. Liao, *Inorg. Chem.*, 2013, **52**, 7380–7386; (*c*) S. Petoud, G. Muller, E. G. Moore, J. Xu, J. Sokolnicki, J. P. Riehl, U. N. Le, S. M. Cohen and K. N. Raymond, *J. Am. Chem. Soc.*, 2007, **129**, 77–83; (*d*) Y.-G. Huang, B.-L. Wu, D.-Q. Yuan, Y.-Q. Xu, F.-L. Jiang and M.-C. Hong, *Inorg. Chem.*, 2007, **46**, 1171–1176.

18 (*a*) X.-J. Feng, H.-Y. Han, Y.-H. Wang, L.-L. Li, Y.-G. Li and E.-B. Wang, *CrystEngComm*, 2013, **15**, 7267–7273; (*b*) C. Ritchie, E. G. Moore, M. Speldrich, P. Kogerler and C. Boskovic, *Angew. Chem., Int. Ed.*, 2010, **49**, 7702–7705.

19 (*a*) T. Yamase in *Chapter 243 Luminescence of Polyoxometallolanthanoates and Photochemical Nano-Ring Formation* ed. J. J.-C. G. B. Karl, A. Gschneidner and K. P. Vitalij, Elsevier, 2009, vol. 39, pp. 297–356; (*b*) T. Yamase, *Chem. Rev.*, 1998, **98**, 307–326.

20 E. Álvarez, M. E. Zayas, J. Alvarado-Rivera, F. Félix-Domínguez, R. P. Duarte-Zamorano and U. Caldiño, *J. Lumin.*, 2014, **153**, 198–202.

21 G. R. Choppin and D. R. Peterman, *Coord. Chem. Rev.*, 1998, **174**, 283–299.

22 (*a*) J. Zhao, D. Shi, L. Chen, Y. Li, P. Ma, J. Wang and J. Niu, *Dalton Trans.*, 2012, **41**, 10740–10751; (*b*) H. An, Z. Han and T. Xu, *Inorg. Chem.*, 2010, **49**, 11403–11414; (*c*) X. Wang, Y. Guo, Y. Li, E. Wang, C. Hu and N. Hu, *Inorg. Chem.*, 2003, **42**, 4135–4140; (*d*) G. Blasse, *J. Chem. Phys.*, 1966, **45**, 2356–2360.

23 S. Quici, M. Cavazzini, G. Marzanni, G. Accorsi, N. Armaroli, B. Ventura and F. Barigelletti, *Inorg. Chem.*, 2005, **44**, 529–537.

24 (*a*) G. Seeta Rama Raju, E. Pavitra and J. S. Yu, *Phys. Chem. Chem. Phys.*, 2014, **16**, 18124–18140; (*b*) M. Tong, Y. Liang, G. Li, Z. Xia, M. Zhang, F. Yang and Q. Wang, *Opt. Mater.*, 2014, **36**, 1566–1570.

25 W.-B. Sun, B.-L. Han, P.-H. Lin, H.-F. Li, P. Chen, Y.-M. Tian, M. Murugesu and P.-F. Yan, *Dalton Trans.*, 2013, **42**, 13397–13403.

26 S.-Y. Lin, L. Zhao, Y.-N. Guo, P. Zhang, Y. Guo and J. Tang, *Inorg. Chem.*, 2012, **51**, 10522–10528.

27 (*a*) C. Benelli and D. Gatteschi, *Chem. Rev.*, 2002, **102**, 2369–2388; (*b*) H. Zhang, S.-Y. Lin, S. Xue, C. Wang and J. Tang, *Dalton Trans.*, 2014, **43**, 6262–6268.

28 (*a*) Y. Wan, L. Zhang, L. Jin, S. Gao and S. Lu, *Inorg. Chem.*, 2003, **42**, 4985–4994; (*b*) J. Niu, K. Wang, H. Chen, J. Zhao, P. Ma, J. Wang, M. Li, Y. Bai and D. Dang, *Cryst. Growth Des.*, 2009, **9**, 4362–4372.

29 U. Kortz, M. G. Savelieff, B. S. Bassil and M. H. Dickman, *Angew. Chem., Int. Ed.*, 2001, **40**, 3384–3386.

30 G. M. Sheldrick, *SADABS—Bruker AXS area detector scaling and absorption version 2008/2001*, University of Göttingen, Germany, 2008.

31 (*a*) G. M. Sheldrick, *SHELXS97, Program for Crystal Structure Solution*, University of Göttingen, Germany, 1997; (*b*) G. M. Sheldrick, *SHELXL97, Program for Crystal Structure Refinement*, University of Göttingen, Germany, 1997.